ISSN 1674-1056
http://cpb.iphy.ac.cn
http://iopscience.iop.org/cpb
中国物理 B
Chinese Physics
中国物理 Chinese Physics B

Magneto-transport properties of thin flakes of Weyl semiconductor tellurium

Nan Zhang(张南), Bin Cheng(程斌), Hui Li(李惠), Lin Li(李林), and Chang-Gan Zeng(曾长淦)
Citation: Chin. Phys. B, 2021, 30 (**8**): 087304. DOI: 10.1088/1674-1056/ac0a5e
Journal homepage: http://cpb.iphy.ac.cn; http://iopscience.iop.org/cpb

What follows is a list of articles you may be interested in

Bound in continuum states and induced transparency in mesoscopic demultiplexer with two outputs

Z Labdouti, T Mrabti, A Mouadili, E H El Boudouti, F Fethi, and B Djafari-Rouhani
Chin. Phys. B, 2020, 29 (**12**): 127301. DOI: 10.1088/1674-1056/abad23

Progress on 2D topological insulators and potential applications in electronic devices

Yanhui Hou(侯延辉), Teng Zhang(张腾), Jiatao Sun(孙家涛), Liwei Liu(刘立巍), Yugui Yao(姚裕贵), Yeliang Wang(王业亮)
Chin. Phys. B, 2020, 29 (**9**): 097304. DOI: 10.1088/1674-1056/aba9c5

Improvement of valley splitting and valley injection efficiency for graphene/ferromagnet heterostructure

Longxiang Xu(徐龙翔), Wengang Lu(吕文刚), Chen Hu(胡晨), Qixun Guo(郭奇勋), Shuai Shang(尚帅), Xiulan Xu(徐秀兰), Guanghua Yu(于广华), Yu Yan(岩雨), Lihua Wang(王立华), Jiao Teng(滕蛟)
Chin. Phys. B, 2020, 29 (**7**): 077304. DOI: 10.1088/1674-1056/ab8db2

Comparative study on transport properties of N-, P-, and As-doped SiC nanowires: Calculated based on first principles

Ya-Lin Li(李亚林), Pei Gong(龚裴), Xiao-Yong Fang(房晓勇)
Chin. Phys. B, 2020, 29 (**3**): 037304. DOI: 10.1088/1674-1056/ab6c4c

Tunneling magnetoresistance in ferromagnet/organic-ferromagnet/metal junctions

Yan-Qi Li(李彦琪), Hong-Jun Kan(阚洪君), Yuan-Yuan Miao(苗圆圆), Lei Yang(杨磊), Shuai Qiu(邱帅), Guang-Ping Zhang(张广平), Jun-Feng Ren(任俊峰), Chuan-Kui Wang(王传奎), Gui-Chao Hu(胡贵超)
Chin. Phys. B, 2020, 29 (**1**): 017303. DOI: 10.1088/1674-1056/ab5d02

RAPID COMMUNICATION

Magneto-transport properties of thin flakes of Weyl semiconductor tellurium*

Nan Zhang(张南)[1,2], Bin Cheng(程斌)[1,2], Hui Li(李惠)[3], Lin Li(李林)[1,2,†], and Chang-Gan Zeng(曾长淦)[1,2,‡]

[1] International Center for Quantum Design of Functional Materials, Hefei National Laboratory for Physical Sciences at the Microscale, and Synergetic Innovation Center of Quantum Information & Quantum Physics, University of Science and Technology of China, Hefei 230026, China

[2] CAS Key Laboratory of Strongly Coupled Quantum Matter Physics, Department of Physics, University of Science and Technology of China, Hefei 230026, China

[3] Key Laboratory of Structure and Functional Regulation of Hybrid Materials of Ministry of Education, Institutes of Physical Science and Information Technology, Anhui University, Hefei 230601, China

(Received 7 June 2021; revised manuscript received 7 June 2021; accepted manuscript online 11 June 2021)

As an elemental semiconductor, tellurium has recently attracted intense interest due to its non-trivial band topology, and the resulted intriguing topological transport phenomena. In this study we report systematic electronic transport studies on tellurium flakes grown via a simple vapor deposition process. The sample is self-hole-doped, and exhibits typical weak localization behavior at low temperatures. Substantial negative longitudinal magnetoresistance under parallel magnetic field is observed over a wide temperature region, which is considered to share the same origin with that in tellurium bulk crystals, *i.e.*, the Weyl points near the top of valence band. However, with lowering temperature the longitudinal magnetoconductivity experiences a transition from parabolic to linear field dependency, differing distinctly from the bulk counterparts. Further analysis reveals that such a modulation of Weyl behaviors in this low-dimensional tellurium structure can be attributed to the enhanced inter-valley scattering at low temperatures. Our results further extend Weyl physics into a low-dimensional semiconductor system, which may find its potential application in designing topological semiconductor devices.

Keywords: Weyl physics, tellurium flakes, negative longitudinal magnetoresistance

PACS: 73.63.−b, 75.47.−m, 73.61.Cw, 73.20.Fz **DOI:** 10.1088/1674-1056/ac0a5e

Tellurium (Te) is a narrow gap (~ 0.32 eV)[1,2] semiconductor with a noncentrosymmetric crystal structure formed by one-dimensional (1D) van der Waals bonded chiral chains. As a versatile material, Te has been widely studied for its intriguing electronic, optical, and piezoelectric properties.[3–5] Recently, there is increasing attention to the exploration of possible non-trivial topological properties of such an elemental semiconductor.[1,6–12] This is due to the fact that the strong spin–orbit coupling and broken inversion symmetry make Te an ideal platform to realize bulk Weyl bands and related Weyl physics.[1,7,8] Actually, the existence of Weyl points deep in the valence band has been experimentally verified via angle-resolved photoemission spectroscopy (ARPES) characterizations.[9] Theoretical studies further revealed that a Weyl semimetal phase emerges in Te by closing its bulk bandgap under external perturbations like high pressure,[1,7,8] as evidenced by the observation of an anomaly in Shubnikov–de Haas oscillations near the critical pressure of topological phase transition.[11] Furthermore, our previous experiments[13] demonstrated typical transport signatures of Weyl physics in self-hole-doped semiconducting Te crystals, such as the negative longitudinal magnetoresistance (NLMR) in the presence of parallel electric and magnetic fields. The Weyl point located at ~ 0.2 eV below the valence band maximum is considered to be responsible for these observations.[13] As a "Weyl semiconductor" combining the advantages of the topological band structure and semiconducting character, Te is a promising platform for both the fundamental research of Weyl physics and the development of topological semiconductor devices.

Compared with bulk crystals, the fabrication of low-dimensional structures facilitates the integration of Weyl physics with modern semiconductor industry, as well as improves the tunability of device performance via various measures, such as electrostatic gating, optical illumination, uniaxial strain, *etc.* The single elemental composition of Te is also beneficial for the growth of low-dimensional structures with high quality. On the other hand, the quantum confinement effect and the modified scattering processes in low-dimensional Te may lead to Weyl transport features differing from the bulk

*Project supported by the Strategic Priority Research Program of the Chinese Academy of Sciences (Grant No. XDC07010000), the National Natural Science Foundation of China (Grant Nos. 11974324, U1832151, 11804326, and 11904001), the National Key Research and Development Program of China (Grant No. 2017YFA0403600), the Anhui Initiative Fund in Quantum Information Technologies (Grant No. AHY170000), and the Fund from the Hefei Science Center, Chinese Academy of Sciences (Grant No. 2020HSC-UE014).

†Corresponding author. E-mail: lilin@ustc.edu.cn

‡Corresponding author. E-mail: cgzeng@ustc.edu.cn

© 2021 Chinese Physical Society and IOP Publishing Ltd

counterpart. Related explorations will pave the way to deeper understanding of Weyl physics. However, previous works on low-dimensional Te mainly focused on basic electronic and optical properties in 1D nanostructures,[4] and field-effect and quantum transport performance in thin Te flakes grown by liquid phase method.[12,14–19]

In this work, via a simple low-temperature physical vapor deposition (PVD) method, high-quality single-crystalline Te flakes are successfully fabricated. Systematic electronic transport measurements are conducted on samples with typical thickness of 30 nm–50 nm. In these self-hole-doped Te flakes, negative magnetoresistance (*MR*) is observed under perpendicular field in the low-field range, which can be explained by the two-dimensional (2D) weak-localization effect. Moreover, large non-saturated negative *MR* under parallel field, *i.e.* the NLMR effect, is observed over a wide temperature range. This observation is ascribed to the chiral anomaly induced by the Weyl band topology of Te, consistent well with the case of bulk crystals.[13] Further analysis reveals that in such a low-dimensional structure, details of the as-observed NLMR behavior are remarkably modulated, manifesting as the transition from parabolic to linear field dependency of the longitudinal magnetoconductivity (MC) with lowering temperature.

Figure 1(a) shows the chiral structure of trigonal Te, in which the helical chains spiral around axes parallel to the *c* axis and are arranged in a hexagonal array in the *a*–*b* plane. The space group is $P3_121$-D_3^4 or $P3_221$-D_3^6 depending on the rotation direction of the helical chain. Te flakes are grown on Si/SiO_2 substrates using the PVD technique (see Note 1 in the supplementary material for materials and methods), as schematically shown in the inset of Fig. S1(a) in the supplementary material. The typical morphologies of the as-grown Te microstructures are shown in the scanning electron microscope (SEM) image in Fig. 1(b) (see also Fig. S1(a) in the supplementary material for the larger-scale image). It is clear that two different types of Te microstructures are obtained, *i.e.*, the high-density microrods on the bottom and sparsely distributed flakes on the top. The overall x-ray diffraction (XRD) spectrum matches well with the standard powder XRD pattern of trigonal Te (JCPDF card No. 36-1452), demonstrating the crystalline quality of the samples. Normally, Te prefers to grow along the *c* direction to form 1D structures like nanorods and nanotubes, due to its highly anisotropic crystal structure. Te flakes are generally realized via high-temperature vapor phase process[20] or liquid phase method.[14,15] Here the obtaining of thin flakes using such a low-temperature PVD method may rely on the bottom microrods serving as special nucleation sites. The in-plane size of the flakes can reach to tenths of micrometers, and the thickness is normally around tenths of nanometers, as typically shown in the atomic force microscopy (AFM) image (Fig. 1(d)). Specially, clear atomic step morphology can be probed in a portion of Te flakes (Fig. S1(d) in the supplementary material), implying the 2D growth mode. The high single-crystalline quality of these flakes can be verified from the high-resolution scanning transmission electron microscopy (STEM) image shown in the inset of Fig. 1(d), via which the surface of the Te flake is determined to be the *a*–*c* plane. The lattice parameters are determined to be $a = b = 4.64$ Å, $c = 6.18$ Å.

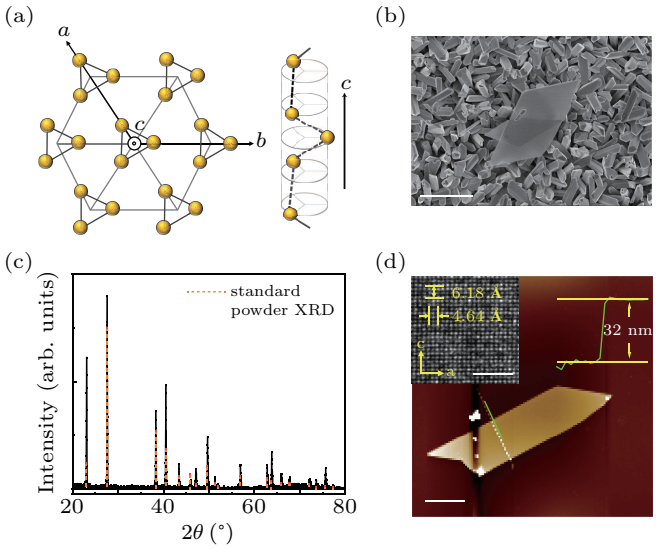


Fig. 1. (a) Crystal structure of trigonal Te. (b) SEM image of Te microstructures grown on a Si/SiO_2 substrate. The scale bar is 5 μm. (c) Overall XRD pattern of the as-grown Te microstructures. (d) AFM image of ∼ 32-nm thick Te flake (sample #1). The scale bar is 5 μm. Inset: typical STEM pattern of the Te flake. The scale bar is 2 nm.

To study the transport properties of the as-grown Te flakes, a standard Hall bar device is then fabricated via the standard electron beam lithography, and the optical image of the device is shown in the inset of Fig. 2(a). During the measurements the current is applied along the long axis of the Te flakes. Below we will present the explicit results for one particular flake (sample #1) with thickness of ∼ 32 nm, and the main features discussed below are also observed in other samples (Fig. S2 in the supplementary material). Figure 2(a) shows the temperature (*T*)-dependent resistance (*R*). With decreasing *T* from 300 K to 2 K, *R* decreases first and then increases continuously, with the minimum occurring at $T \sim 140$ K. Similar *R*–*T* behavior has also been seen in Te bulk crystals,[13] but the minimum of the *R*–*T* curve occurred at a temperature nearly 100 K lower than that of the Te flakes here. Hall data shown in Figs. 2(c) and 2(d) demonstrate that the Te flake is hole-doped. Besides, the nonlinearity of Hall curves becomes obvious at temperatures above 100 K (Fig. 2(d)), which is most likely due to the two-carrier effect. For simplicity, the carrier density is estimated via the linear fitting of the Hall curve ranging from 12 T to 14 T, as detailed in Note 2 in the supplementary material. Both the carrier density and mobility decrease with lowering temperature below

$\sim$ 30 K (Fig. 2(b)). This behavior can be ascribed to the carrier freeze-out effect, which is a common feature for semiconductors at low temperatures.[21] Here the carrier freeze-out effect means the carriers become localized around impurities or defects at low temperatures, rendering the deionization of the donors or acceptors. In other words, the thermal excitation of carriers gets significantly suppressed, leading to the reduction of both the carrier density and the mobility. There are two possible origins accounting for the p-type nature of Te flakes, *i.e.* surface accumulation layers[22,23] or bulk vacancies serving as acceptors.[13,24] However, the surface carriers can hardly freeze out and the conductance should be nearly constant at low temperatures,[22,25] incompatible with our observations. In addition, the carrier density of this sample is about two orders of magnitude higher than that of Te bulks grown by a similar PVD method, which is most likely due to the existence of larger amounts of Te vacancies.[13,24]

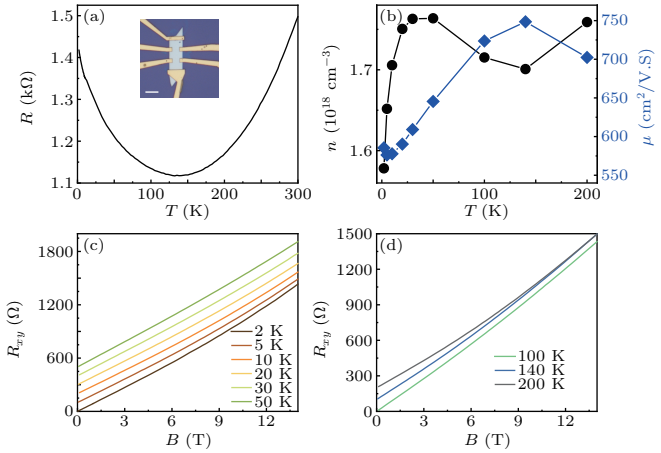


Fig. 2. (a) Temperature-dependent resistance of the Te flake. Inset: optical image of the device. The scale bar is 5 μm. (b) Temperature-dependent carrier density and mobility. The carrier density is extracted from the linear fitting of the Hall curve ranging from 12 T to 14 T. (c) and (d) Hall resistance measured at different temperatures (vertically shifted for clarity).

Figure 3(a) shows the transverse *MR* (defined as $(R(B) - R(0))/R(0) \times 100\%$) under perpendicular magnetic fields across a temperature range of 2 K–200 K. Overall, typically positive *MR* effect is demonstrated, with no signatures of saturation at magnetic fields up to 14 T. The positive *MR* achieves its maximum at $\sim$ 140 K, and the value at 14 T is $\sim$ 37%. Notably, negative transverse *MR* emerges in the small field regime (typically below $\sim$ 2 T) at temperatures below $\sim$ 30 K. The magnitude of negative *MR* increases with decreasing temperature, which is reminiscent of the weak localization effect. Generally, for Weyl systems possessing non-trivial band topology, weak antilocalization is more likely to happen.[26] However, it has been theoretically predicted that increasing the weight of inter-valley scattering will strengthen the localization tendency, leading to the emergence of weak localization effect.[26] Note that the occurrence of inter-valley scattering requires a large momentum transfer that is usually induced by atomically sharp defects like vacancies. For our Te flakes, the Te vacancies could promote the inter-valley scattering, and thus lead to the observation of the weak localization effect at low temperatures. For further exploration, the transverse MC ($\Delta\sigma(B) = \sigma(B) - \sigma(B = 0)$) is calculated and then fitted using the following Hikami–Larkin–Nagaoka (HLN) formula that describes the quantum corrections to the MC:[27]

$$\Delta\sigma(B) = \alpha \frac{e^2}{2\pi^2\hbar} F\left(\frac{B}{B_\varphi}\right),$$
$$F(x) = \psi\left(\frac{1}{2} + \frac{1}{x}\right) + \ln(x), \quad (1)$$

where the factor α is normally equal to 1 (-0.5) for the case of weak localization (antilocalization),[27] ψ is the digamma function, $B_\varphi = \hbar/(4eL_\varphi^2)$ is the characteristic field related to the phase coherence, and L_φ is the phase coherence length. As demonstrated in Fig. 3(b), low-field transverse MC at 2 K can be well fitted via formula (1). In addition, the obtained α (1.027) nearly equals 1, verifying the weak localization origin of the small field transverse *MR*. It is noted such weak localization effect is only observed in the Te flakes rather than the bulk crystals, which is probably related to the quantum confinement.[28] The extracted L_φ at 2 K ($\sim$ 44 nm) is larger than the sample thickness ($\sim$ 32 nm), further supporting the 2D character of the present Te flake.

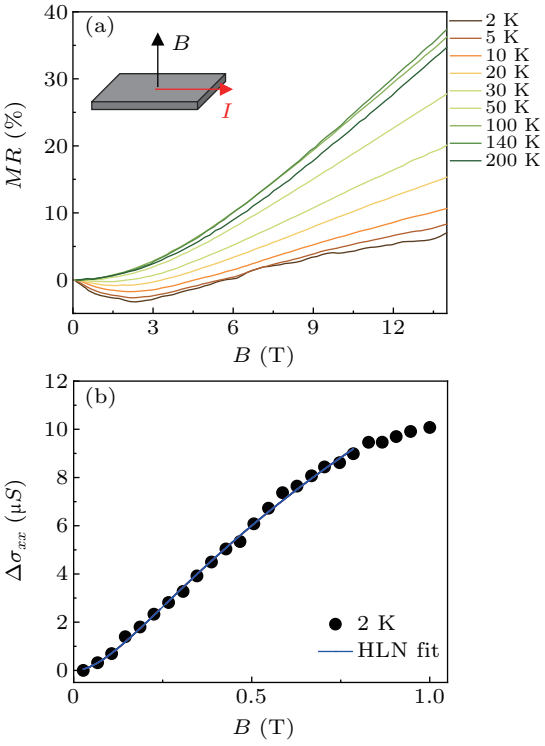


Fig. 3. (a) *MR* measured at temperatures ranging from 2 K to 200 K for *B* perpendicular to *I*. (b) Low-field MC at 2 K and the corresponding HLN fitting curve (dark blue line) using formula (1).

When the magnetic field is parallel to the current ($B \| I$), negative *MR* behavior is clearly demonstrated over the whole measured field range (Fig. 4(a)). The NLMR effect degrades

with increasing temperature due to the thermal effect, but remains observable up to 200 K (Fig. 4(b)). At $T = 2$ K and $B = 14$ T, the highest negative MR of $\sim 11.3\%$ is obtained. As is known, NLMR is rarely observed in a non-magnetic material and can serve as one of the transport signatures of Dirac/Weyl materials.[29–41] In our previous work,[13] various topological transport phenomena, including the NLMR, the planar Hall effect, as well as the intriguing log-periodic magneto-oscillations, were obtained in Te bulk crystals, and can be well attributed to the nontrivial band topology. Due to the broken inversion symmetry and strong spin–orbit coupling, the crossings of spin-splitting bands lead to the formation of multiple Weyl points in the bulk bands of Te.[1,7,8] Utilizing band structure calculations assisted by ARPES characterizations, the Weyl point located at ~ 0.2 eV below the valence band maximum can contribute a non-zero Berry curvature around the Fermi level, and thus exerts significant impact on the versatile topological transport behaviors.[13] For the present Te flakes possessing higher hole density, the distance between the Fermi level and the Weyl point becomes smaller, therefore the observed NLMR could be reasonably attributed to the special Weyl bands. Moreover, the negative MR at $\theta = 0°$ (*i.e.*, $B \| I$, θ is the angle between B and I) is largely suppressed at $\theta = 30°$ (Fig. S3 in the supplementary material), further supporting its chiral anomaly origin.

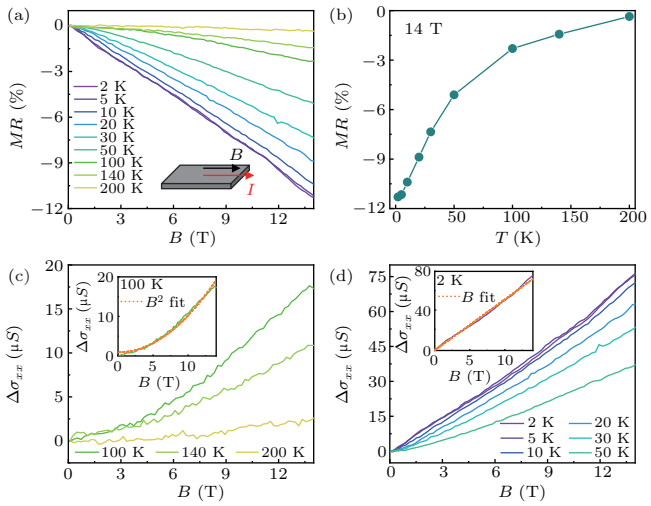


Fig. 4. (a) MR measured at temperatures ranging from 2 K to 200 K for $B \| I$. (b) Temperature dependence of longitudinal MR at 14 T. (c) MC at 100 K–200 K for $B \| I$. Inset: parabolic fitting of MC at 100 K. (d) MC at 2 K–50 K for $B \| I$. Inset: linear fitting of MC at 2 K.

Figures 4(c) and 4(d) show the calculated longitudinal MC ($\Delta\sigma(B) = \sigma(B) - \sigma(B = 0)$) for $B \| I$. Due to the absence of the weak antilocalization effect and the negligible conventional MR, the longitudinal MC is almost fully dominated by the chiral anomaly. Moreover, the MC exhibits a unique field dependence transition, *i.e.*, B^2 dependency at high temperatures (Fig. 4(c)), and linear field dependency at low temperatures (Fig. 4(d)). Such transition has never been observed in bulk crystals and is further supported by power law fitting of the longitudinal MC at various temperatures (Fig. S4 in the supplementary material).

In the theoretical work by Son and Spivak,[40] the chiral anomaly induced longitudinal MC is proportional to B^2 in the semi-classical region, which has been widely observed in topological semimetals,[29,31–34,36–39] while it turns into a linear field dependence in the quantum limit region. In Fig. 4(c), $\Delta\sigma$ at high temperatures can be well fitted using a simplified formula[36] $\sigma = \sigma_0 + a \cdot B^2$, where σ is the zero-field conductivity, consistent well with the case in the semi-classical region. However, the linear field dependence of $\Delta\sigma$ at low temperatures (Fig. 4(d)) occurs over the full field range, which thus cannot be interpreted by the quantum-limit origin. Moreover, the critical field for the quantum limit is estimated to be ~ 50 T at 2 K according to the extracted carrier density of the sample,[31] which further excludes the quantum-limit origin.

Note that in the theory developed by Son and Spivak,[40] there is an important assumption that the intra-valley scattering determines the transport performance while the inter-valley scattering is negligible.[42] Ji *et al.*[43,44] further explored the effects of both intra-valley and inter-valley scattering induced by the screened Coulomb potential, and revealed that the linear longitudinal MC is actually closely relevant to the enhanced contribution of the inter-valley scattering. Considering the relatively high carrier density of Te flakes arising from the large amounts of Te vacancies, the screened Coulomb potential may effectively affect the magnetotransport behaviors by introducing both the intra-valley scattering and inter-valley scattering.[43] As the temperature decreases, the inter-valley scattering takes a more important role in the transport behavior, as evidenced by the emergence of weak localization as well as the violation of Kohler's rule (see Note 3 and Fig. S6 in the supplementary material), leading to a transition from parabolic to linear field dependence of the longitudinal MC. Even though detailed microscopic analyses are still needed, the observation of linear longitudinal MC in low-dimensional quantum-confined Te flakes is most likely due to the enhanced contribution of the inter-valley scattering at low temperatures.

In summary, high-quality crystalline Te flakes are grown through a simple low-temperature PVD method. Robust negative MR in parallel magnetic field is clearly demonstrated and ascribed to the chiral anomaly induced by the Weyl band structure of Te, consistent with the case for Te bulks. Detailed analyses reveal that the longitudinal MC experiences a transition of the field dependence with varying temperatures, which is suggested to originate from the modulation of Weyl behaviors induced by the enhanced inter-valley scattering at low temperatures. The realization of Weyl physics in such a low-dimensional semiconductor system will definitely enrich the study of topological materials, and also offer an ideal platform for the development of high-tunable and easy-integrated

topological electronic/optoelectronic devices in the future.

References

[1] Hirayama M, Okugawa R, Ishibashi S, Murakami S and Miyake T 2015 *Phys. Rev. Lett.* **114** 206401
[2] Anzin V B, Eremets M I, Kosichkin Y V, Nadezhdinskii A I and Shirokov A M 1977 *Phys. Status Solidi A* **42** 385
[3] Gerlach E and Grosse P 1979 *The Physics of Selenium and Tellurium* (New York: USA Springer)
[4] He Z, Yang Y, Liu J and Yu S 2017 *Chem. Soc. Rev.* **46** 2732
[5] Wu W, Qiu G, Wang Y, Wang R and Ye P 2018 *Chem. Soc. Rev.* **47** 7203
[6] Agapito L A, Kioussis N, Goddard W A and Ong N P 2013 *Phys. Rev. Lett.* **110** 176401
[7] Tsirkin S S, Souza I and Vanderbilt D 2017 *Phys. Rev. B* **96** 045102
[8] Murakami S, Hirayama M, Okugawa R and Miyake T 2017 *Sci. Adv.* **3** e1602680
[9] Nakayama K, Kuno M, Yamauchi K, Souma S, Sugawara K, Oguchi T, Sato T and Takahashi T 2017 *Phys. Rev. B* **95** 125204
[10] Tsirkin S S, Puente P A and Souza I 2018 *Phys. Rev. B* **97** 035158
[11] Ideue T, Hirayama M, Taiko H, Takahashi T, Murase M, Miyake T, Murakami S, Sasagawa T and Iwasa Y 2019 *Proc. Natl. Acad. Sci. USA* **116** 25530
[12] Qiu G, Niu C, Wang Y, Si M, Zhang Z, Wu W and Ye P D 2020 *Nat. Nanotechnol.* **15** 585
[13] Zhang N, Zhao G, Li L, Wang P, Xie L, Cheng B, Li H, Lin Z, Xi C, Ke J, Yang M, He J, Sun Z, Wang Z, Zhang Z and Zeng C 2020 *Proc. Natl. Acad. Sci. USA* **117** 11337
[14] Wang Y, Qiu G, Wang R, Huang S, Wang Q, Liu Y, Du Y, Goddard W A, Kim M J, Xu X, Ye P D and Wu W 2018 *Nat. Electron.* **1** 228
[15] Amani M, Tan C, Zhang G, Zhao C, Bullock J, Song X, Kim H, Shrestha V R, Gao Y, Crozier K B, Scott M and Javey A 2018 *ACS Nano* **12** 7253
[16] Du Y, Qiu G, Wang Y, Si M, Xu X, Wu W and Ye P D 2017 *Nano Lett.* **17** 3965
[17] Qiu G, Wang Y, Nie Y, Zheng Y, Cho K, Wu W and Ye P D 2018 *Nano Lett.* **18** 5760
[18] Niu C, Qiu G, Wang Y, Zhang Z, Si M, Wu W and Ye P D 2020 *Phys. Rev. B* **101** 205414
[19] Ren X, Wang Y, Xie Z, Xue F, Leighton C and Frisbie C D 2019 *Nano Lett.* **19** 4738
[20] Wang Q, Safdar M, Xu K, Mirza M, Wang Z and He J 2014 *ACS Nano* **8** 7497
[21] Neamen D A 2011 *Semiconductor Physics and Devices: Basic Principles* (New York: McGraw-Hill)
[22] Von Klitzing K and Landwehr G 1971 *Solid State Commun.* **9** 2201
[23] Berezovets V A, Farbshtein I I and Shelankov A L 1984 *JETP Lett.* **39** 74
[24] Tanuma S 1954 *Sci. Rep. Res. Inst., Tohoku Univ., Ser. A* **6** 159
[25] Englert T, von Klitzing K, Silbermann R and Landwehr G 1977 *Phys. Status Solidi B* **81** 119
[26] Lu H and Shen S 2017 *Front. Phys.* **12** 127201
[27] Hikami S, Larkin A I and Nagaoka Y 1980 *Prog. Theor. Phys.* **63** 707
[28] Datta S 1997 *Electronic transport in mesoscopic systems* (Cambridge: Cambridge University Press)
[29] Xiong J, Kushwaha S K, Liang T, Krizan J W, Hirschberger M, Wang W, Cava R J and Ong N P 2015 *Science* **350** 413
[30] Li C, Wang L, Liu H, Wang J, Liao Z and Yu D 2015 *Nat. Commun.* **6** 10137
[31] Li H, He H, Lu H, Zhang H, Liu H, Ma R, Fan Z, Shen S and Wang J 2016 *Nat. Commun.* **7** 10301
[32] Zhang C, Xu S, Belopolski I, Yuan Z, Lin Z, Tong B, Bian G, Alidoust N, Lee C, Huang S, Chang T R, Chang G, Hsu C, Jeng H T, Neupane M, Sanchez D S, Zheng H, Wang J, Lin H, Zhang C, Lu H, Shen S, Neupert T, Zahid Hasan M and Jia S 2016 *Nat. Commun.* **7** 10735
[33] Liu E, Sun Y, Kumar N, Muechler L, Sun A, Jiao L, Yang S, Liu D, Liang A, Xu Q, Kroder J, Süß V, Borrmann H, Shekhar C, Wang Z, Xi C, Wang W, Schnelle W, Wirth S, Chen Y, Goennenwein S T B and Felser C 2018 *Nat. Phys.* **14** 1125
[34] Huang X, Zhao L, Long Y, Wang P, Chen D, Yang Z, Liang H, Xue M, Weng H, Fang Z, Dai X and Chen G 2015 *Phys. Rev. X* **5** 031023
[35] Hirschberger M, Kushwaha S, Wang Z, Gibson Q, Liang S, Belvin Carina A, Bernevig B A, Cava R J and Ong N P 2016 *Nat. Mater.* **15** 1161
[36] Li Q, Kharzeev D E, Zhang C, Huang Y, Pletikosić I, Fedorov A V, Zhong R D, Schneeloch J A, Gu G D and Valla T 2016 *Nat. Phys.* **12** 550
[37] Wang Y, Liu E, Liu H, Pan Y, Zhang L, Zeng J, Fu Y, Wang M, Xu K, Huang Z, Wang Z, Lu H, Xing D, Wang B, Wan X and Miao F 2016 *Nat. Commun.* **7** 13142
[38] Guo C Y, Wu F, Wu Z Z, Smidman M, Cao C, Bostwick A, Jozwiak C, Rotenberg E, Liu Y, Steglich F and Yuan H Q 2018 *Nat. Commun.* **9** 4622
[39] Zheng G, Lu J, Zhu X, Ning W, Han Y, Zhang H, Zhang J, Xi C, Yang J, Du H, Yang K, Zhang Y and Tian M 2016 *Phys. Rev. B* **93** 115414
[40] Son D T and Spivak B Z 2013 *Phys. Rev. B* **88** 104412
[41] Burkov A A 2014 *Phys. Rev. Lett.* **113** 247203
[42] Goswami P, Pixley J H and Das Sarma S 2015 *Phys. Rev. B* **92** 075205
[43] Ji X, Lu H, Zhu Z and Su G 2017 *AIP Adv.* **7** 105003
[44] Ji X, Lu H, Zhu Z and Su G 2018 *J. Appl. Phys.* **123** 203901